

AURA-CVC: Autonomous Ultrasound-guided Robotic Assistance for Central Venous Catheterization

Deepak Raina¹, Lidia Al-Zogbi¹, Brian Teixeira², Vivek Singh², Ankur Kapoor², Thorsten Fleiter³, Muyinatu A. Lediju Bell^{1†}, Vinciya Pandian^{4†}, Axel Krieger^{1*†}

¹Johns Hopkins University, Baltimore, MD, USA.

²Siemens Healthineers, Princeton, NJ, USA.

³University of Maryland, Baltimore, MD, USA.

⁴Penn State University, University Park, PA, USA.

*Corresponding author(s). E-mail(s): axel@jhu.edu;

†These authors advised this work equally.

Abstract

Purpose: Central venous catheterization (CVC) is a critical medical procedure for vascular access, hemodynamic monitoring, and life-saving interventions. Its success remains challenging due to the need for continuous ultrasound-guided visualization of a target vessel and approaching needle, which is further complicated by anatomical variability and operator dependency. Errors in needle placement can lead to life-threatening complications. While robotic systems offer a potential solution, achieving full autonomy remains challenging. In this work, we propose an end-to-end robotic-ultrasound-guided CVC pipeline, from scan initialization to needle insertion.

Methods: We introduce a deep-learning model to identify clinically relevant anatomical landmarks from a depth image of the patient's neck, obtained using RGB-D camera, to autonomously define the scanning region and paths. Then, a robot motion planning framework is proposed to scan, segment, reconstruct, and localize vessels (veins and arteries), followed by the identification of the optimal insertion zone. Finally, a needle guidance module plans the insertion under ultrasound guidance with operator's feedback. This pipeline was validated on a high-fidelity commercial phantom across 10 simulated clinical scenarios.

Results: The proposed pipeline achieved 10 out of 10 successful needle placements on the first attempt. Vessels were reconstructed with a mean error of 2.15 mm,

and autonomous needle insertion was performed with an error less than or close to 1 mm.

Conclusion: To our knowledge, this is the first robotic CVC system demonstrated on a high-fidelity phantom with integrated planning, scanning, and insertion. Experimental results show its potential for clinical translation.

Keywords: Robotic ultrasound, ultrasound-guided interventions, central venous catheterization, motion-planning

1 Introduction

Central venous catheterization (CVC) is widely performed in intensive care, trauma, major surgery, parenteral nutrition, and hemodialysis, with over 7 million annual placements in the U.S. [1]. It is typically performed at the internal jugular (IJ), subclavian, or femoral veins, with IJ preferred for its superficial location, consistent anatomy, and reduced risk. Ultrasound-guided CVC is now the clinical standard [2]. The procedure involves ultrasound scanning to identify vessels, estimating insertion point, and advancing the needle. Major complications occur in 3% of placements (i.e., 4.4 pneumothorax, 16.2 arterial puncture, 2.8 arterial cannulation per 1000 cases) [3]. Despite ultrasound guidance, continuous simultaneous visualization of a vessel and needle is difficult due to narrow imaging planes and vessel “roll-away” during advancement. These challenges highlight the need for advanced technologies to reduce workload and improve safety.

Robot-assisted ultrasound (RUS) has emerged as a promising solution to enhance precision, minimize human error, and improve outcomes in diagnostic and interventional applications [4–6]. Several handheld or semi-automated needle insertion devices have been developed to improve workspace, accuracy, and force resistance [7–9]. For example, CathBot [8] enables clinicians to initiate insertion by pushing a handle, after which the device autonomously completes cannulation. While effective for peripheral vascular access on the forearm, its design has limited CVC utility due to anatomical complexities of neck, chest, or groin sites. Other robotic systems demonstrated teleoperated insertion, initiated from manually marked regions [10, 11] or vessel boundaries [12]. Efforts have recently shifted towards autonomy with advanced robotics, imaging, and sensor-guided needles [13], reinforced by the first-in-human image-guided system in [14], showing 100% success with no complications in 19 attempts. Similarly, Hong *et al.* [15] developed a percutaneous insertion robot compensating for patient motion via real-time visual-servoing. Neubach *et al.* [16] introduced closed-loop steering using ultrasound-estimated tip position with tissue stiffness modeling. Xu *et al.* [17] proposed slice-guidance interpolating preoperative scans to compensate liver motion. Chatelain *et al.* [18] used particle filtering to track flexible needles for real-time closed-loop control. While these approaches [15–18] advance motion compensation, they lack integrated intra-operative planning for full autonomy.

Zettinig *et al.* [19] annotated pre-interventional plans in CT/MRI and proposed a 3D visual-servoing framework with multi-modal registration to update needle targets under motion. Kojcev *et al.* [20] developed a dual-arm ultrasound-guided system integrating force-controlled acquisition, registration, vision-based control, and tracking, though planning still relied on manual region selection. Bell *et al.* [21] and Gubbi *et al.* [22] demonstrated photoacoustic-based visual servoing. Cheng *et al.* [23] used impedance sensing to detect vascular entry. Koskinopoulou *et al.* [24] combined ultrasound and bioimpedance in a dual-arm system for vessel localization and venipuncture detection. While these systems [19–23] demonstrate end-to-end procedures, scanning was typically initialized from predefined poses or required experts to review intra-operative CT/MRI images.

In contrast, our system achieves fully autonomous scan initialization using feedback from a low-cost, widely accessible RGB-D camera, eliminating the need for expert intervention or expensive intra-operative imaging. In addition, many of the initial system validations were performed with simplified vascular access phantoms that do not capture the anatomical and physiological complexity of humans. In this work, we validate our initial pipeline on a high-fidelity phantom model, moving one step closer to in-human procedures. Key contributions of this work include:

1. First robotic pipeline that autonomously performs key CVC steps: intra-operative planning, scanning, anatomical localization, and needle placement
2. A novel method to predict the optimal scanning region and trajectory using only a single depth image from an RGB-D camera.
3. A fully automated robotic scanning and vascular reconstruction for localization of vein and artery, followed by supervised needle guidance.
4. Feasibility demonstration of the system on a near-realistic CVC phantom for IJ vein access across 10 diverse clinical scenarios.

2 Materials and Methods

2.1 Experimental testbed

The experimental testbed (Fig. 1) includes: (1) a 6-DoF UR10e robotic arm (Universal Robots, Denmark) with 10 kg payload and inbuilt force-torque sensor; (2) a C3 HD3 curved ultrasound probe (Clarius, Canada) mounted via extended attachment (although linear probes are preferred for CVC, we used a convex probe for its wider field of view and availability during prototyping); (3) an Ubuntu PC and a laptop with NVIDIA RTX 4090 (16GB) and 1090 (12GB) for system control and deep learning-based feedback; (4) a RealSense D415 RGB-D camera (Intel, USA) for localization; (5) a custom 2-DoF needle insertion mechanism adapted from [12], providing linear and angular control, compatible with any robotic arm with adequate payload, equipped with an 18-gauge, 15 cm bevel-tipped needle (Cook Medical, USA) to constantly align its trajectory with the ultrasound plane, ensuring continuous visualization (unlike manual procedures, which rely on clinician skill to infer the needle tip); and (6) a CVC Blue Phantom (CAE, USA) for validation, offering realistic upper thorax and

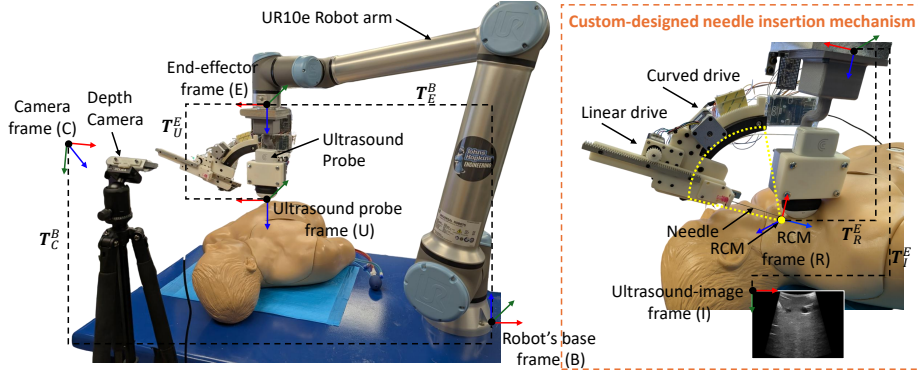


Fig. 1: Overview of the experimental testbed showing the robotic system setup, a close-up view of the needle insertion mechanism, and the defined reference frames. The corresponding homogeneous transformation matrices, denoted as \mathbf{T}_1^2 , represent the pose of frame 1 relative to frame 2.

neck anatomy, including major vessels and landmarks for CVC. Note that the communication across system components was established via ROS2 (Robot Operating System).

Let \mathbf{T}_1^2 denote the homogeneous transformation matrix that expresses the pose of frame 1 relative to frame 2. The frames used in the system are: robot's base (B), end-effector (E), camera (C), ultrasound probe (U), remote center-of-motion (R), and ultrasound image (I) (see Fig. 1). The 3D position in world coordinate system (p_B) of a given pixel in the 2D ultrasound image (p_I) is calculated using:

$$\mathbf{p}_B = \mathbf{T}_E^B \cdot \mathbf{T}_U^E \cdot \mathbf{T}_I^U \cdot \mathbf{p}_I \quad (1)$$

where \mathbf{T}_I^U is the transformation from the ultrasound probe frame to the pixel values in the image frame and is given by

$$\mathbf{T}_I^U = \begin{bmatrix} S_x & 0 & 0 & 0 \\ 0 & S_y & 0 & 0 \\ 0 & 0 & 1 & 0 \\ 0 & 0 & 0 & 1 \end{bmatrix} \begin{bmatrix} I_x \\ I_y \\ 0 \\ 1 \end{bmatrix} \quad (2)$$

where $S_x = S_y = 0.15436 \text{ mm}$ is the pixel spacing (scaling factor) provided by the Clarius Mobile Health software development kit and (I_x, I_y) is the given pixel value in x - and y -direction of the image frame.

2.2 Pipeline

Our pipeline is shown in Fig. 2. During initialization, system calibration was performed by estimating \mathbf{T}_C^B via hand-eye calibration and \mathbf{T}_U^E using the classical $AX = XB$ method [25], with a cross-wire phantom in a water bath. The region encompassing IJ vein and carotid artery was then autonomously identified from depth images, followed

by robotic ultrasound scanning, vessel segmentation, 3D reconstruction, insertion point selection, and closed-loop needle guidance for puncture.

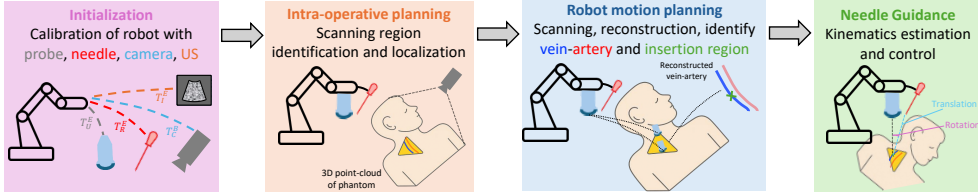


Fig. 2: Our pipeline has four phases: the initialization phase, intra-operative planning, robot motion planning, and the needle guidance

2.3 Intra-operative planning

2.3.1 Overview

Clinicians often define a triangular region using the suprasternal notch (SN), sternocleidomastoid (SCM) midpoint, and lateral clavicle (LC), known as Sedillot's triangle, to guide IJ vein access [26]. Inspired by this, we used SN, LC, and anterior hyoid bone tip (HT) to define a similar region, with HT chosen for its prominence and absence of SCM in the phantom. This region ensured presence of the IJ vein. These Landmarks were identified using a deep learning model, which were then used to plan the scanning path, as described below.

2.3.2 Anatomical landmark prediction network

The anatomical landmark prediction network required a depth image of the neck-torso region. Synchronized depth and color images were first captured, followed by HSV thresholding to segment the head and torso of the phantom, then depth filtering for a refined 3D point cloud. This segmented point-cloud was the network's input (Fig. 3(a)). Following [27], we trained a Dense-UNet [28] to predict internal landmarks from depth images. The encoder-decoder architecture had four dense blocks of four convolutional layers (Fig. 3(b)), with batch normalization and ReLU after each convolution except the final layer. The dataset comprised 4,912 depth images of real humans with diverse habitus, sex, and skin tone. Landmarks were manually annotated using co-registered RGB-D data and verified against anthropometric measurements. The model was trained for 300 epochs with Adam optimizer ($lr = 0.001$, batch = 32) minimizing Adaloss, predicting 33 landmarks, including three critical to CVC, with additional landmarks to improve accuracy.

2.3.3 Scanning region and path estimation

The scanning region was defined by a triangular region formed by 3 predicted landmarks (SN, LC, and HT). This region was projected onto the phantom surface using

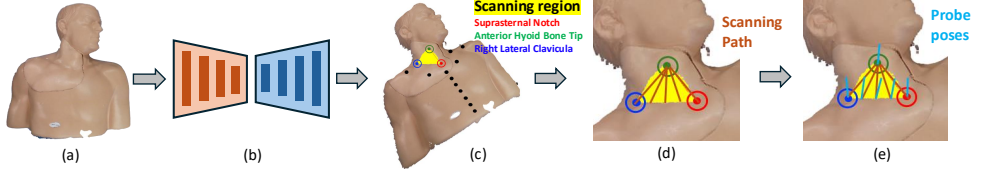


Fig. 3: (a) Depth image of the phantom’s neck and torso. (b) Landmark prediction network for anatomical localization. (c) Scanning region (yellow patch) on the neck is defined using three predicted anatomical landmarks. (d) Planned scanning paths are shown as maroon lines. (e) Probe poses along the scanning paths, with surface normals at each pose illustrated by light-blue lines.

the Open3D Python library, as shown in Fig. 3(c). To scan within this region, we defined straight-line paths from the triangle’s base (SN–LC) to its apex (HT), aligning with the IJ vein’s orientation. Initial paths connected HT to LC and HT to SN. Additional scanning paths were created by dividing the SN–LC line into equal intervals and connecting lines from HT to these points, yielding a dense scan pattern for accurate vessel detection (Fig. 3(d)). Scanning was initiated along the midpoint-to-HT path because this path aligned with the expected anatomical course of the IJ vein, offering a clinically representative initial view. This path also provided a reliable starting point across different patient positioning due to its geometric symmetry.

2.4 Robot motion planning

2.4.1 Overview

Once the scanning region was identified, the pipeline generated a robot trajectory for scanning and localizing the vein-artery, as illustrated in Fig. 4. After robotic scanning, the vein was localized and centered in the ultrasound image to ensure consistent spatial referencing. Then the robot was re-oriented for sagittal plane insertion, which offered full needle shaft visibility. A collision check was performed using the CAD model and phantom point cloud. If a collision was detected in the sagittal orientation, the robot iteratively adjusted its pivot angle in transverse view about the point of contact by 5° until a collision-free pose was found. Upon confirming clearance, the robot transitioned to the sagittal plane for needle insertion.

2.4.2 Scanning trajectory

The scanning path generated on the phantom in Section 2.3 defined the robot trajectory as:

$$\mathcal{T} = [\mathbf{P}_i, \dots, \mathbf{P}_n] \quad (3)$$

Each pose transform \mathbf{P}_* was defined as $[\vec{x}, \vec{y}, \vec{z}, \vec{t}]$, where \vec{t} is the translation (or position) vector and $\vec{x}, \vec{y}, \vec{z}$ are unit vectors for orientation. The start and end of the scanning path define \mathbf{P}_0 and \mathbf{P}_n , respectively. The normal \vec{z} of phantom was

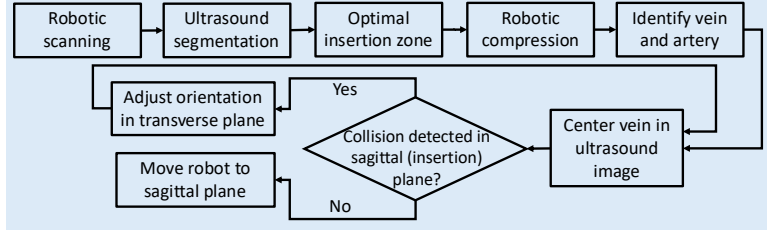


Fig. 4: Robot motion planning workflow to identify optimal insertion point, localize vein-artery, and move to sagittal (insertion) plane while avoiding collision.

computed using Open3D and aligned with the end-effector's normal \vec{z}_e using:

$$\vec{z} = \begin{cases} \vec{z}, & \text{if } \vec{z} \cdot \vec{z}_e > 0 \\ -\vec{z}, & \text{otherwise} \end{cases} \quad (4)$$

The x-axis \vec{x} was aligned with the phantom's major axis, and \vec{y} was computed as:

$$\vec{y} = \frac{\vec{z} \times \vec{x}}{\|\vec{z} \times \vec{x}\|} \quad (5)$$

Intermediate poses were interpolated between \mathbf{P}_0 and \mathbf{P}_n using the UR driver. ROS2 and URScript executed the trajectory in hybrid force-position mode with 5 N force along the z -axis of the probe, chosen as the minimum force required to ensure sufficient acoustic contact while minimizing tissue deformation. During scanning, a rosbag recorded poses and images pairs $(\mathbf{P}_i, \mathbf{I}_i)$ for each frame, described as follows to enable accurate vessel reconstruction:

$$\mathbf{D} = \{(\mathbf{P}_i, \mathbf{I}_i), \dots, (\mathbf{P}_n, \mathbf{I}_n)\} \quad (6)$$

2.4.3 Identifying optimal insertion plane

The acquired 2D US frames were segmented to reconstruct vessels and plan needle insertion. A deep learning model from prior work [29] was used to extract vessel center-points and areas from each frame. Ideally, insertion should occur where both vessels (vein and artery) are clearly visible for confident and precise targeting. To determine the insertion point, the robot insertion pose (\mathbf{P}) was selected from $\mathbf{P}_i, \dots, \mathbf{P}_n$ as that corresponding to the maximum combined area of the two vessels. This selection criterion is illustrated in Fig. 5. The robot was finally moved to pose \mathbf{P} , and the corresponding ultrasound frame was re-segmented.

2.4.4 Vein-artery localization

Veins are difficult to distinguish from arteries, as both appear morphologically similar in ultrasound images. While clinicians typically use Doppler ultrasound to differentiate vessels based on blood flow, this method requires manual tuning, favorable imaging

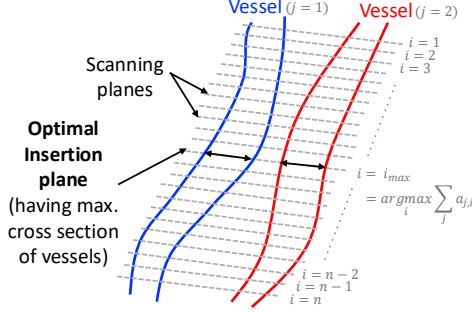


Fig. 5: Criteria for selecting optimal needle insertion plane. $a_{j,i}$ is the area of the j^{th} vessel in image I_i from dataset \mathcal{D} (Eq. (6)), with j limited to 2 to exclude noise, as only two vascular structures are expected to be visible.

conditions, and expertise, making it less practical in portable or low-cost devices where Doppler functionality or detectable flow is absent. To address these limitations, our system employs a compression-based method that exploits differences in vascular compliance, whereby veins exhibit greater deformation than arteries under low external pressure.

The robot applied controlled compression by gradually increasing the contact force from 5 N to 10 N, then decreasing back to 5 N, while recording an ultrasound video. Note that this compression was applied only briefly for classification. The maximum applied force of 10 N is considered clinically safe and does not induce patient discomfort. Segmented vessel areas and centroids were extracted from the recorded sequence. Then, KMeans clustering was used, which grouped vessel centroids into two clusters based on their spatial proximity. Area changes across the compression cycle were computed for each cluster, with the one showing greater deformation identified as the vein, and the other as the artery. The centroid of the vein cluster was stored as a reference. Later, at the insertion pose, the robot captured a new ultrasound frame, segmented the vessels, and identified the vein by finding the centroid closest to the saved reference, with the remaining vessel labeled as the artery.

2.5 Needle guidance

The robotic needle mechanism has two degrees of freedom: (i) rotation (θ) to align the needle with the desired insertion angle, and (ii) translation (d) to advance the needle to the target depth. These desired angle and depth of needle are computed from the kinematic relationship between the IJ vein center and the RCM of the needle mechanism (see Fig. 1).

Let $p^{VC} = [x^{VC}, y^{VC}, z^{VC}]$ and $p^{RCM} = [x^{RCM}, y^{RCM}, z^{RCM}]$ denote the 3D coordinates of the vein center and RCM, respectively, in the robot base frame. The vein center was first identified from the segmented region in the transverse ultrasound plane and then tracked in the sagittal plane. The desired insertion angle θ is defined as the angle between the line connecting the RCM to the vein center and the vertical

z -axis of the robot's end-effector frame, with an offset to account for the mechanism design:

$$\theta = \tan^{-1} \left(\frac{x^{VC} - x^{RCM}}{z^{VC} - z^{RCM}} \right) - \theta_{\text{offset}}, \quad (7)$$

where $\theta_{\text{offset}} = 18.21^\circ$ is the initial tilt of the needle guide relative to the robot z -axis. The insertion depth is given by the Euclidean distance between the vein center and the RCM:

$$d = |p^{VC} - p^{RCM}|. \quad (8)$$

To minimize targeting error, a closed-loop controller was implemented. The controller adjusted the translational motion of the needle to minimize the perpendicular distance between the needle tip and pre-defined vein centerline during advancement. Since the needle orientation was fixed prior to insertion, this control ensured safe puncture and in-vein positioning. The proportional controller used a gain of 0.5. At present, the vein centerline was marked manually once in the sagittal ultrasound view, and the needle tip location was manually identified after each advancement step. The needle was advanced until the tip reached within 1 mm of the centerline.

3 Experiments and Results

3.1 Overview

To comprehensively evaluate the robustness and clinical relevance of our system, we conducted 10 experiments under varied simulated clinical scenarios. These included: (i) five experiments (Exp. 1-5) with different phantom orientations representing common patient positions during CVC (e.g., Trendelenburg, head turns, torso tilt); and (ii) five additional experiments (Exp. 6-10) introducing random perturbations by adding Gaussian noise ($\mu = 0$, $\sigma = 0.01$) to the scanning path to simulate real-world uncertainties such as patient motion or breathing. Fig. 6 illustrates the five baseline orientations, while Table 1 summarizes the corresponding phantom-to-robot frame transformations and noise-induced deviations.

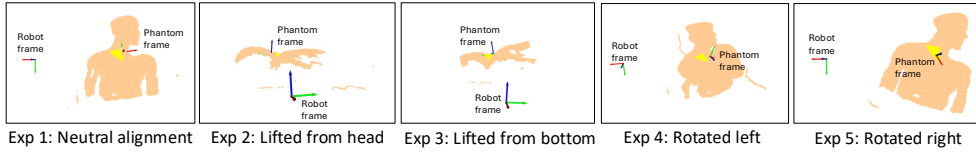


Fig. 6: Illustrating experiments 1–5, each with a different phantom orientation relative to the robot base to assess system's robustness to patient positioning in different clinical scenarios.

Table 1: Exp. 1-5 corresponds to scenarios with different orientations (in *deg.*) of phantom with respect to (w.r.t) robot base and Exp. 6-10 corresponds to scenarios with different amounts of deviations (in *mm*) added to the start and end point of the scanning path.

Exp.	Rotation of phantom w.r.t robot			Exp.	Start Deviation		End Deviation	
	Roll	Pitch	Yaw		Δx	Δy	Δx	Δy
1	-3.220	-1.711	-173.129	6	+3.295	-4.298	-8.128	+7.024
2	6.011	-0.376	-177.914	7	+5.385	-17.523	+23.160	-5.776
3	13.003	-0.065	-174.284	8	+3.024	-5.065	-9.509	+1.549
4	4.036	-1.779	122.572	9	-1.270	+6.466	-1.229	-16.543
5	3.016	3.377	155.136	10	-10.250	+6.343	-2.225	-15.113

3.2 Landmark prediction

With 427 test depth images, the mean Euclidean error for 33 landmarks was $13.59\text{ mm} \pm 10.49\text{ mm}$ (95th percentile: 34.26 mm). For the three key CVC landmarks, SN, RLC, and HT, the mean error was $13.88\text{ mm} \pm 11.55$ (95th percentile: 35.35 mm). Table 2 shows detailed results. Although the maximum error reached 34.17 mm , this error did not hinder downstream vessel localization, as the triangular scanning region was large enough to encompass the IJ vein.

Table 2: Mean, standard deviation (S.D.), and 95th percentile error for CVC landmarks.

Landmark	Mean \pm S.D. (95 th Percentile) [mm]
SN	13.03 ± 11.21 (36.96)
RLC	12.77 ± 10.52 (32.09)
HT	15.84 ± 12.91 (37.01)
Average	13.88 ± 11.55 (35.35)

3.3 Vein-artery centerline reconstruction

Fig. 7 shows representative segmentation results of veins and arteries from ultrasound frames. The reconstructed vein and artery centerlines were then obtained by transforming these segmentation outputs in the robot frame using Eq. (1) and compared with the ground truth centerlines extracted from CT scans of the phantom. The CT data was processed using the Vascular Modeling Toolkit in 3D Slicer to extract the centerlines discretized at 1 mm intervals to serve as the ground truth. The reconstructed and ground truth centerlines were aligned using the ICP algorithm (Fig. 8). To assess the accuracy of reconstructed centerlines, we computed their k -nearest neighbors distance with the ground truth center-point, as reported in Table 3.

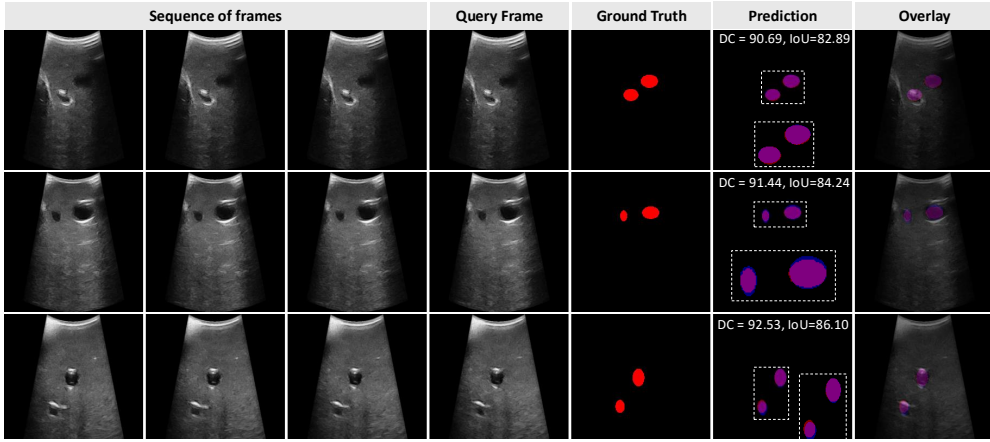


Fig. 7: Comparison of segmentation network predictions with ground truth on the test set. Predicted regions are shown in blue, ground truth in red, and their overlap in magenta. White boxes highlight zoomed-in views of the overlapping regions.

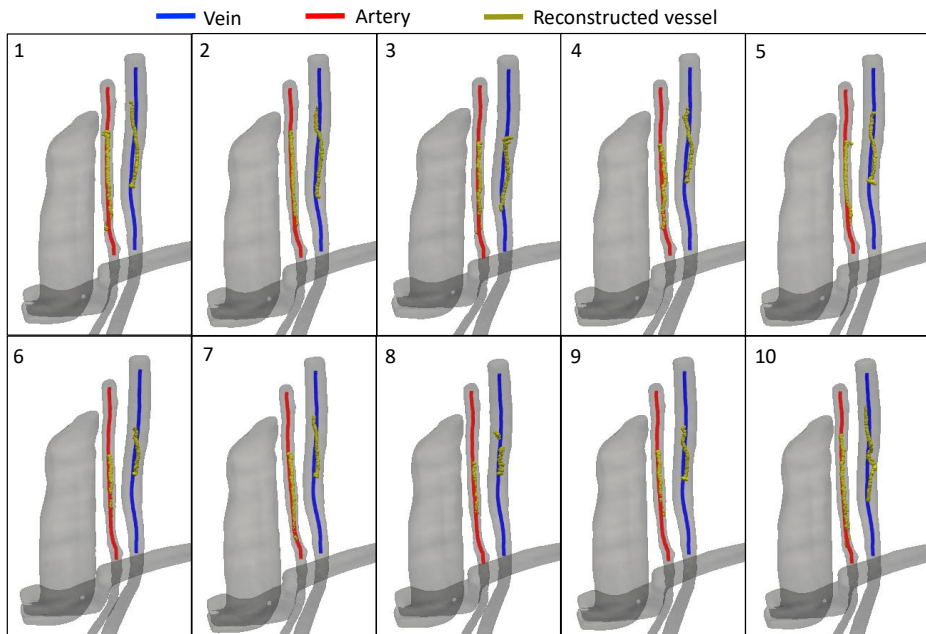


Fig. 8: Comparison of 3D reconstruction of centerline of vein and artery (both marked with yellow color) with their ground truths (blue color for vein and red color for artery) for the 10 experiments

Table 3: Reconstruction accuracy reported as mean, maximum, and standard deviation (S.D.) errors (in mm) between reconstructed and ground-truth vein and artery center-lines.

Exp.	Vein			Artery		
	Mean	Max.	S.D.	Mean	Max.	S.D.
1	3.28	5.06	0.98	1.21	2.24	0.43
2	3.13	5.05	0.96	1.05	2.49	0.47
3	2.74	4.56	0.78	1.08	2.49	0.39
4	3.32	4.93	0.96	1.20	2.32	0.44
5	3.28	5.21	1.14	1.01	3.74	0.57
Avg (1-5)	3.15	4.96	0.96	1.11	2.66	0.46
6	3.28	4.94	0.80	1.01	2.77	0.44
7	3.29	4.57	0.87	1.02	2.05	0.32
8	3.10	6.12	1.23	1.08	2.46	0.51
9	3.38	4.26	0.54	1.08	1.79	0.28
10	3.33	5.71	0.88	1.19	3.16	0.45
Avg (6-10)	3.28	5.12	0.86	1.08	2.45	0.40

3.4 Needle targeting accuracy

The targeting accuracy of the system was evaluated by computing the error between the target and final needle tip position. The 3D positions of the target point and needle tip were calculated using Eq. (1) from the marked pixel locations in the sagittal view. After each experiment, an expert (co-author VP) marked the needle location and IJ vein (center point and boundary) in the ultrasound frame. This evaluation was performed first in the sagittal view after insertion. The probe was then removed, and manual handheld scanning collected transverse and sagittal views of the insertion region. Catheter insertion was performed to confirm vein access. Ultrasound videos from hand-held scanning and catheter insertion were later analyzed by the expert to verify safe insertion into the IJ vein.

Fig. 9 shows the targeted 3D vein position and final needle tip location. Table 4 reports the corresponding errors under the ‘Evaluation via Robot’ column. Fig. 10 shows expert annotations in selected transverse and sagittal frames from recorded ultrasound videos. The transverse view confirmed the needle tip remained inside the vein boundary, while the sagittal view re-confirmed that puncture was safe, with the tip remaining close to the centerline. Catheter insertion was also confirmed.

Errors were computed as the distance between needle tip and vein center-point in the transverse view, and as the perpendicular distance to the vein centerline in the sagittal view. These distances were recorded in pixels and later converted to millimeters using the scaling factor described in Section 2.1. Table 4 summarizes these results under the ‘Evaluation via Expert’ column.

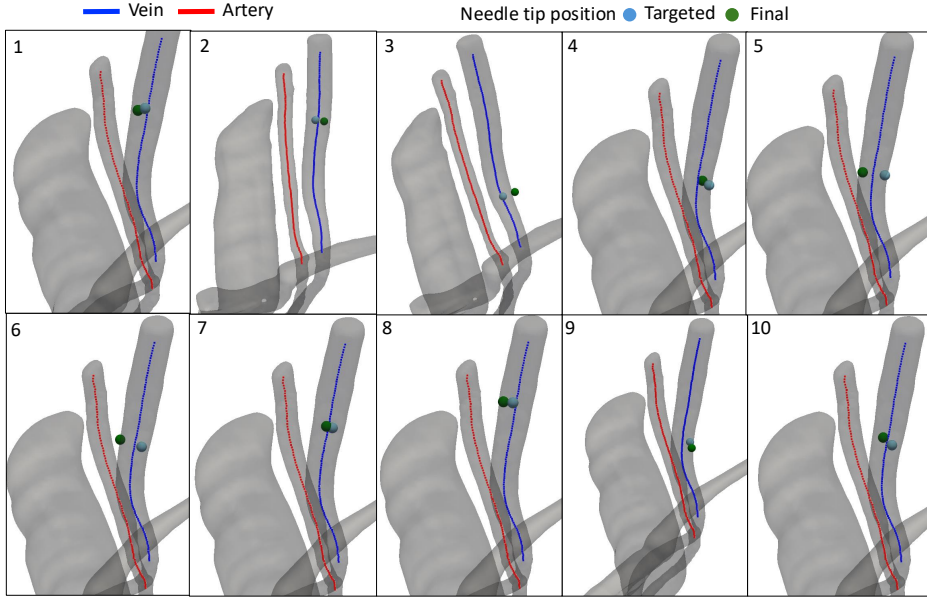


Fig. 9: Comparing the 3D needle tip position (green sphere) with the targeted vein center-point (blue sphere)

Table 4: Error between the needle tip and vein center-point or center-line, evaluated with robot kinematics after insertion (Fig. 9) and expert annotations (Fig. 10). Insertion success is marked using '✓' for safe needle insertion, bleeding of blue-color fluid (artery has red-color fluid), and catheter insertion.

Evaluation via →	Error between needle tip and IJ vein's				Insertion Success		
	center-point (mm)		center-line (mm)		Safe insertion	Blue bleed	Catheter insertion
	Robot	Expert	Robot	Expert			
1	1.87	1.66	0.39	0.45	✓	✓	✓
2	3.08	1.24	1.01	1.14	✓	✓	✓
3	6.85	1.24	0.90	0.72	✓	✓	✓
4	0.31	3.25	0.47	0.78	✓	✓	✓
5	5.26	5.09	0.32	0.96	✓	✓	✓
Mean (1-5)	3.47	2.49	0.62	0.63			
S.D. (1-5)	2.61	1.49	0.31	0.29			
6	4.50	2.17	1.15	0.46	✓	✓	✓
7	1.27	2.49	0.25	1.52	✓	✓	✓
8	1.24	2.06	0.80	1.85	✓	✓	✓
9	2.19	1.57	1.38	1.32	✓	✓	✓
10	2.18	2.01	0.31	0.69	✓	✓	✓
Mean (6-10)	2.28	2.06	0.78	1.17			
S.D. (6-10)	1.33	0.29	0.50	0.52			

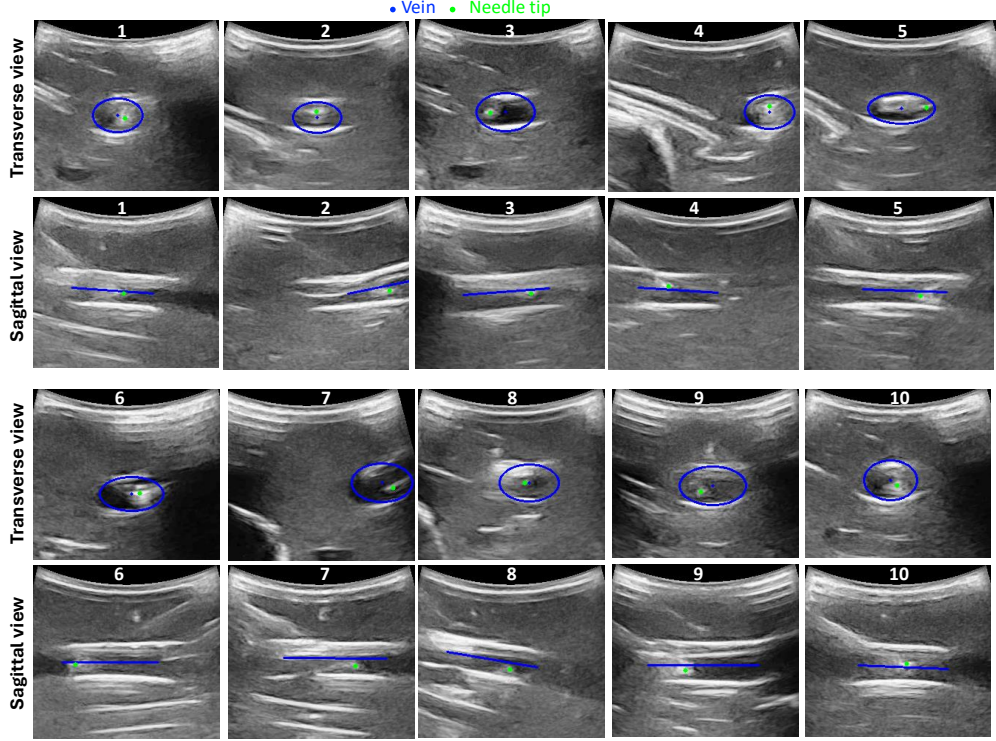


Fig. 10: Expert’s annotations on transverse and sagittal ultrasound views acquired with hand-held scanning after insertion

4 Discussion

We presented phantom experiments to evaluate vessel centerline reconstruction and needle targeting accuracy. The proposed pipeline and validation serve as a foundation for a clinically deployable system. Performance was generally acceptable, with three aspects of less-than-ideal performance explained below.

First, the reconstructed vein showed higher mean \pm S.D. error (Table 3) due to two factors: (1) the compressibility of the vein under force-controlled scanning, which was not accounted for in the CT ground truth, and (2) use of a convex rather than linear probe, which is typically preferred for CVC. Nonetheless, combined vein-artery error (2.15 mm) indicates the 2D-ultrasound-to-3D calibration preserved spatial accuracy, which is essential for needle entry planning.

Second, needle targeting accuracy (Fig. 9) showed tip alignment near the IJ vein centerline, with average errors of 0.62 mm and 0.78 mm for Exp. 1–5 and 6–10 (Table 4). These values fall within the 1 mm threshold used in the controller (Section 2.5). Slightly higher errors arose in Exp. 2, 6 and 9 due to bending of the 150 mm long needle, yet reported values remained within the vein radius (3.24–6.16 mm).

Third, for expert-evaluated manual scans, mean \pm SD errors from the center-point were 2.49 ± 1.49 mm and 2.06 ± 0.29 mm for Exp. 1–5 and 6–10, respectively, with largest errors in Exp. 4–5 from unavoidable needle tilting. The mean \pm SD errors from the centerline were 0.63 ± 0.29 mm and 1.17 ± 0.52 mm, for Exp. 1–5 and 6–10, respectively, increasing with induced trajectory noise but decreasing in Exp. 10 due to unpredictable bending. Besides needle deflection, part of the error can be attributed to ultrasound calibration inaccuracies (1.64 ± 0.84 mm). Nonetheless, across all experiments, mean needle tip error relative to the vessel centerline was 0.90 ± 0.42 mm, within the vein radius, confirming effective insertion. For reference, Chen *et al.* [12] reported 0.9 ± 0.29 mm accuracy in a pork phantom.

Three limitations should be addressed in future work. First, reducing the footprint of needle mechanism would improve positioning flexibility, which is particularly important for obese patients or those with shorter necks where sagittal access is not possible. Second, independent probe–needle motion could allow steeper insertion angles, better aligning with clinical preferences such as the lateral short-axis insertion emphasized in [30]. Finally, manual marking of the needle tip in ultrasound images currently limits real-time use; a future pipeline will integrate automated needle tip detection and tracking to improve autonomy and reduce operator dependence.

Future work will use anatomically representative phantoms [29] or fresh cadavers to validate our system under more realistic physiological conditions. Our immediate next step would be validation of insertion zone selection on human subjects (without insertion). Beyond validation, we also aim to incorporate real-time tissue–needle interaction models and compensation strategies into our framework.

5 Conclusion

We have shown that the effective integration of intra-operative planning, anatomical identification, and needle guidance could enable the end-to-end robotic execution of central venous catheterization. To the best of our knowledge, this is the first time depth camera feedback has been used to identify the scanning region, thereby eliminating the need to rely on medical experts or intra-operative CT/MRI scans. Another novelty of this work is the use of force-guided robotic motion to identify the vein and artery based on their compressibility, thereby reducing the reliance on complex ultrasound imaging feedback (multi-class segmentation or Doppler ultrasound). The success of this system can be observed from the successful needle placement with an error below or close to 1 mm.

Acknowledgements. This work is partially supported by the Agency for Healthcare Research and Quality (AHRQ) under Grant No. 7R18HS029124-03 (previously 5R18HS029124-03), the National Science Foundation (NSF) CAREER Award under Grant No. 2144348, the NSF Future of Work at the Human-Technology Frontier (FW-HTF) Award No. 2222716, the NSF Alan T. Waterman Award No. 2431810, and the Malone Center for Engineering in Healthcare Postdoctoral Fellowship.

References

- [1] Kehagias, E., Galanakis, N., Tsetis, D.: Central venous catheters: Which, when and how. *The British Journal of Radiology* **96**(1151), 20220894 (2023)
- [2] Govindan, S., Snyder, A., Flanders, S.A., Chopra, V.: Peripherally inserted central catheters in the icu: a retrospective study of adult medical patients in 52 hospitals. *Critical care medicine* **46**(12), 1136–1144 (2018)
- [3] Teja, B., Bosch, N.A., Diep, C., Pereira, T.V., Mauricio, P., Sklar, M.C., Sankar, A., Wijeysundera, H.C., Saskin, R., Walkey, A., *et al.*: Complication rates of central venous catheters: a systematic review and meta-analysis. *JAMA Internal Medicine* **184**(5), 474–482 (2024)
- [4] Biswas, P., Sikander, S., Kulkarni, P.: Recent advances in robot-assisted surgical systems. *Biomedical Engineering Advances* **6**, 100109 (2023)
- [5] Raina, D., Singh, H., Saha, S.K., Arora, C., Agarwal, A., Chandrashekara, S., Rangarajan, K., Nandi, S.: Comprehensive telerobotic ultrasound system for abdominal imaging: Development and in-vivo feasibility study. In: 2021 International Symposium on Medical Robotics (ISMR), pp. 1–7 (2021). IEEE
- [6] Raina, D., Balakuntala, M.V., Kim, B.W., Wachs, J., Voyles, R.: Coaching a robotic sonographer: Learning robotic ultrasound with sparse expert's feedback. *IEEE Transactions on Medical Robotics and Bionics* (2024)
- [7] Slocum, A., Bassett, E., Karp, J.M., Langer, R.S., Farokhzad, O.C.: Methods and devices for sensing tissues and tissue compartments. Google Patents. US Patent 8,920,388 (2014)
- [8] Cheng, Z., Davies, B.L., Caldwell, D.G., Mattos, L.S.: A hand-held robot for precise and safe pvc. *IEEE Robotics and Automation Letters* **4**(2), 655–661 (2019)
- [9] Ikhsan, M., Tan, K.K., Putra, A.S.: Assistive technology for ultrasound-guided central venous catheter placement. *Journal of Medical Ultrasonics* **45**, 41–57 (2018)
- [10] Zevallos, N., Harber, E., Patel, K., Gu, Y., Sladick, K., Guyette, F., Weiss, L., Pinsky, M.R., Gomez, H., Galeotti, J., *et al.*: Toward robotically automated femoral vascular access. In: 2021 International Symposium on Medical Robotics (ISMR), pp. 1–7 (2021). IEEE
- [11] Zevallos, N., Morales, C.G., Orekhov, A., Rane, T., Gomez, H., Guyette, F.X., Pinsky, M.R., Galeotti, J., Dubrawski, A., Choset, H.: Automatic cannulation of femoral vessels in a porcine shock model. *arXiv preprint arXiv:2506.14467* (2025)

- [12] Chen, S., Wang, F., Lin, Y., Shi, Q., Wang, Y.: Ultrasound-guided needle insertion robotic system for percutaneous puncture. *International Journal of Computer Assisted Radiology and Surgery* **16**, 475–484 (2021)
- [13] Koskinopoulou, M., Cheng, Z., Acemoglu, A., Caldwell, D.G., Mattos, L.S.: Robotic devices for assisted and autonomous intravenous access. *IEEE Transactions on Medical Robotics and Bionics* **5**(2), 170–179 (2023)
- [14] Herlihy, J.P., Cohn, W.E., Ebner, A.: Centrally inserted central catheter placement using a novel, handheld, image-guided, robotic device: Results of initial feasibility trial in patients. *The Journal of Vascular Access*, 11297298241273637 (2025)
- [15] Hong, J., Dohi, T., Hashizume, M., Konishi, K., Hata, N.: An ultrasound-driven needle-insertion robot for percutaneous cholecystostomy. *Physics in Medicine & Biology* **49**(3), 441 (2004)
- [16] Neubach, Z., Shoham, M.: Ultrasound-guided robot for flexible needle steering. *IEEE Transactions on Biomedical Engineering* **57**(4), 799–805 (2009)
- [17] Xu, J., Jia, Z.-z., Song, Z.-j., Yang, X.-d., Chen, K., Liang, P.: Three-dimensional ultrasound image-guided robotic system for accurate microwave coagulation of malignant liver tumours. *The International Journal of Medical Robotics and Computer Assisted Surgery* **6**(3), 256–268 (2010)
- [18] Chatelain, P., Krupa, A., Navab, N.: 3d ultrasound-guided robotic steering of a flexible needle via visual servoing. In: 2015 IEEE International Conference on Robotics and Automation (ICRA), pp. 2250–2255 (2015). IEEE
- [19] Zettinig, O., Frisch, B., Virga, S., Esposito, M., Rienmüller, A., Meyer, B., Hennersperger, C., Ryang, Y.-M., Navab, N.: 3d ultrasound registration-based visual servoing for neurosurgical navigation. *International journal of computer assisted radiology and surgery* **12**, 1607–1619 (2017)
- [20] Kojcev, R., Fuerst, B., Zettinig, O., Fotouhi, J., Lee, S.C., Frisch, B., Taylor, R., Sinibaldi, E., Navab, N.: Dual-robot ultrasound-guided needle placement: closing the planning-imaging-action loop. *International journal of computer assisted radiology and surgery* **11**, 1173–1181 (2016)
- [21] Bell, M.A.L., Shubert, J.: Photoacoustic-based visual servoing of a needle tip. *Scientific Reports* **8**, 15519 (2018)
- [22] Gubbi, M.R., Bell, M.A.L.: Deep learning-based photoacoustic visual servoing: Using outputs from raw sensor data as inputs to a robot controller. In: Proceedings of the IEEE International Conference on Robotics and Automation (ICRA) (2021). IEEE

- [23] Cheng, Z., Davies, B.L., Caldwell, D.G., Mattos, L.S.: A venipuncture detection system for robot-assisted intravenous catheterization. In: 2016 6th IEEE International Conference on Biomedical Robotics and Biomechatronics (BioRob), pp. 80–86 (2016). IEEE
- [24] Koskinopoulou, M., Acemoglu, A., Penza, V., Mattos, L.S.: Dual robot collaborative system for autonomous venous access based on ultrasound and bioimpedance sensing technology. In: 2023 IEEE International Conference on Robotics and Automation (ICRA), pp. 4648–4653 (2023). IEEE
- [25] Kim, C., Chang, D., Petrisor, D., Chirikjian, G., Han, M., Stoianovici, D.: Ultrasound probe and needle-guide calibration for robotic ultrasound scanning and needle targeting. *IEEE Transactions on Biomedical Engineering* **60**(6), 1728–1734 (2013)
- [26] Kosnik, N., Kowalski, T., Lorenz, L., Valacer, M., Sakthi-Velavan, S.: Anatomical review of internal jugular vein cannulation. *Folia Morphologica* **83**(1), 1–19 (2024)
- [27] Teixeira, B., Singh, V., Tamersoy, B., Prokein, A., Kapoor, A.: Automated ct lung cancer screening workflow using 3d camera. In: International Conference on Medical Image Computing and Computer-Assisted Intervention, pp. 423–431 (2023). Springer
- [28] Li, X., Chen, H., Qi, X., Dou, Q., Fu, C.-W., Heng, P.-A.: H-denseunet: hybrid densely connected unet for liver and tumor segmentation from ct volumes. *IEEE transactions on medical imaging* **37**(12), 2663–2674 (2018)
- [29] Al-Zogbi, L., Raina, D., Pandian, V., Fleiter, T., Krieger, A.: Robotic ultrasound-guided femoral artery reconstruction of anatomically-representative phantoms. *arXiv preprint arXiv:2503.06795* (2025)
- [30] Rossi, U.G., Rigamonti, P., Tichà, V., Zoffoli, E., Giordano, A., Gallieni, M., Cariati, M.: Percutaneous ultrasound-guided central venous catheters: the lateral in-plane technique for internal jugular vein access. *The journal of vascular access* **15**(1), 56–60 (2014)